Synergistic Enhancement of Electrocatalytic CO_2 Reduction with Gold Nanoparticles Embedded in Functional Graphene Nanoribbon Composite Electrodes

Cameron Rogers,[†] Wade S. Perkins,[†] Gregory Veber,[†] Teresa E. Williams,[¶] Ryan R. Cloke,[†] and Felix R. Fischer[†,ʃ,||]*

[†]Department of Chemistry, University of California Berkeley, Berkeley, CA 94720, USA.

[¶]The Molecular Foundry, Lawrence Berkeley National Laboratory, Berkeley, CA 94720, USA.

[ʃ]Material Sciences Division, Lawrence Berkeley National Laboratory, Berkeley, CA 94720, USA.

[||]Kavli Energy Nanosciences Institute at the University of California Berkeley and Lawrence Berkeley National Laboratory, Berkeley, California 94720, USA.

ABSTRACT: Regulating the complex environment accounting for the stability, selectivity, and activity of catalytic metal nanoparticle interfaces represents a challenge to heterogeneous catalyst design. Here we demonstrate the intrinsic performance enhancement of a composite material comprised of gold nanoparticles (AuNPs) embedded in a bottom-up synthesized graphene nanoribbon (GNR) matrix for the electrocatalytic reduction of CO_2. Electrochemical studies reveal that the structural and electronic properties of the GNR composite matrix increase the AuNP electrochemically active surface area (ECSA), lower the requisite CO_2 reduction overpotential by hundreds of mV (catalytic onset > –0.2 V vs. reversible hydrogen electrode (RHE)), increase the Faraday efficiency (> 90%), markedly improve stability (catalytic performance sustained over > 24 h), and increase the total catalytic output (>100-fold improvement over traditional amorphous carbon AuNP supports). The inherent structural and electronic tunability of bottom-up synthesized GNR-AuNP composites affords an unrivaled degree of control over the catalytic environment, providing a means for such profound effects as shifting the rate determining step in the electrocatalytic reduction of CO_2 to CO, and thereby altering the electrocatalytic mechanism at the nanoparticle surface.

INTRODUCTION

Inorganic nanostructured materials, primarily realized in the form of nanoparticles (NPs), have emerged as competent heterogeneous catalysts for challenging chemical transformations.[1–4] While nanostructured catalysts promote the industrial scale production of value added chemicals, more recently their characteristics have inspired NP-based water splitting, fuel cell, and carbon dioxide (CO_2) reduction catalysts, relevant to a sustainable clean energy cycle.[5,6] While traditional catalyst design has focused on intrinsic structural parameters like size, shape, and composition of NPs,[7–15] the more complex variables of the nanostructured catalytic environment and the dynamic mass- and energy-transport processes at the solid/liquid or solid/gas interface remain insufficiently understood.[16] A more inclusive model that embraces the multifaceted role of the support along with the demonstrated tunability of NPs themselves offers new opportunities for the design and performance optimization of heterogeneous catalyst systems.[17] Indeed, the structural diversity of chemical environments surrounding catalytically active sites at the surface of NPs are typically described by ensemble measurements,[18–20] and this analytical challenge is further convoluted by the inherent inhomogeneity of common support materials such as carbon black (C_{black}), reduced graphene oxide (rGO), carbon nanotubes (CNTs), or inorganic metal oxides (MO_x) at the nanometer scale, preventing the development of instructive structure-performance relationships. Here we show that by rational bottom-up design of a functional graphene nanoribbon support material it is possible to boost key performance parameters such as stability, selectivity, and activity, thereby enhancing the electrocatalytic reduction of CO_2 by gold nanoparticles (AuNPs) in aqueous solution. Electrochemical measurements further reveal that this molecular-materials support can influence the mechanism for CO_2 reduction at the nanoparticle interface.

AuNPs are appealing CO_2 reduction electrocatalysts as they offer aqueous compatibility and reasonable selectivity for CO_2 reduction to CO, together with the high surface area inherent to metal nanoparticles.[8,13] As electrocatalytic reduction of CO_2 at the surface of metal NPs follows a proton-coupled mechanism, it necessarily faces competing proton reduction, limiting the Faraday efficiency (FE) for CO production.[21,22] Moreover, competent nanoparticle catalysts frequently contend with low activity or prohibitively high overpotential for bulk applications.[6,10,12,23] Most pressing, however, is the issue of catalyst stability, as many nanoparticle electrocatalyst systems deliver strong performance for only minutes before degrading under harsh electrocatalytic conditions.[12,24-27] Efforts to mitigate premature catalyst deactivation have highlighted the role of the support material in stabilizing nanodispersed metals.[25-30] Graphitic support materials in particular have drawn significant interest,

largely because their structure and electronics facilitate strong interaction between the carbon support and metal nanoparticles.[31-35] These strong d-π interactions[32,36-37] lead to enhanced dispersion and stabilization of metal NPs and can serve to modulate the electronic structure at the NP surface.[30,38-39] As such, graphene,[34,40,41] GO,[42] rGO,[43] and CNTs[44-46] have been investigated as nanoparticle support materials, particularly in the contexts of fuel cells[28,33,44,46] and thermal catalysis.[32] While each of these graphitic materials carries certain inherent strengths and limitations, all of them notably lack rational tunability and structural homogeneity on the nanometer scale.

Narrow graphene nanoribbons (GNRs) are an intriguing high-performance material that have recently become accessible through scalable, solution-based bottom-up synthesis.[47-51] GNRs offer structural precision and tunability unrivaled among graphitic materials, since their structure follows deterministically from small molecule precursors readily modified through organic synthesis. Electronic homogeneity follows from structural homogeneity, and as such bottom-up GNRs do not contend with the variable band gaps and metallicity found in CNTs. Combining structural and electronic tunability with mechanical flexibility and a high aspect ratio graphitic topology, bottom-up GNRs are appealing materials for enhancing support-NP interaction and thereby exerting control over catalytic performance and stability. The potential enhancement is not restricted to the mechanical immobilization of metallic NPs within an inert matrix, but takes advantage of charge transfer at the GNR-metal NP interface, a Mott-Schottky heterojunction, that can give rise to superior catalytic performance.[52-60] Inspired by the use of graphitic support materials (e.g. graphene, rGO, CNTs, mesoporous carbon), we explored structurally defined bottom-up synthesized GNRs as a functional support for AuNP electrocatalysis. In the first section of this manuscript we describe how the catalytic environment created by GNR composites enhances AuNP CO_2 reduction across every measure of performance, notably including a dramatic improvement in catalytic stability. Throughout a second section we highlight the molecular tunability inherent to a synthetically-derived GNR support material and how it can be utilized to further enhance catalytic performance, demonstrating the suitability of bottom-up synthesized GNRs as a next-generation support material.

RESULTS AND DISCUSSION

Chevron GNRs (**1**)[47] and cove GNRs (**2a**)[48,61] were synthesized following the bottom-up strategy outlined in Figure 1. While chevron GNR precursor **3** was prepared following a reported procedure,[62] the synthesis of molecular precursors for cove GNRs **4a** and **4b** is depicted in Scheme 1. Knoevenagel condensation of **5** with 1,3-diphenylpropan-2-one yielded the brominated cyclopentadienone **6**. Sonogashira cross-coupling of **6** with ethynyltrimethylsilane followed by deprotection of the TMS group gave the heterobifunctional molecular building block **4a**. The inherent flexibility of a rational bottom-up synthesis of graphene nanoribbons from molecular precursors is illustrated by the synthesis of a **4b**, a derivative of **4a** featuring methyl esters along its edges (Scheme 1). Knoevenagel condensation of **8** with 1,3-bis(4-bromophenyl)propan-2-one gave cyclopentadienone **9**, featuring both iodide and bromide substituents on the aromatic rings. Selective Sonogashira cross-coupling of **9** with ethynyltrimethylsilane yielded the dibromocyclopentadienone **10**. Pd-catalyzed carbonylation of **10** in MeOH followed by deprotection of the TMS group with AgF gave the molecular precursor for methyl ester functionalized cove GNRs **4b**.[63,64]

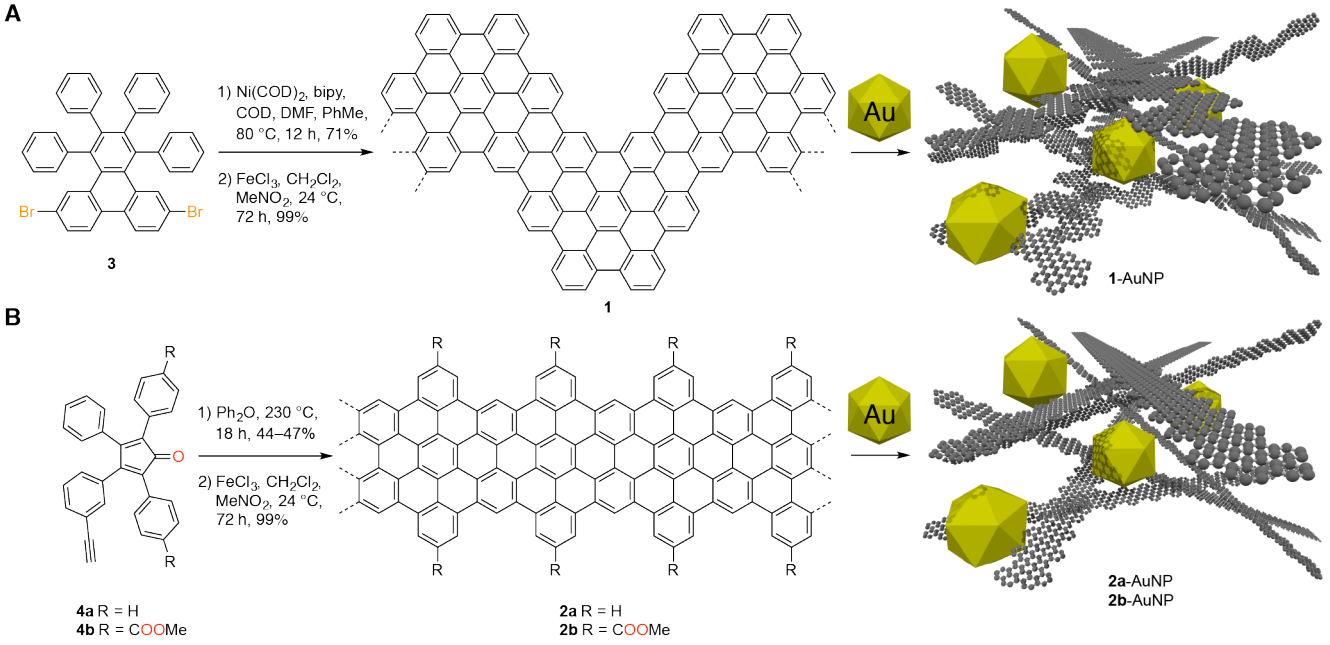

Figure 1. Design and bottom-up synthesis of GNR-AuNP composite materials. (A) Synthesis of chevron GNRs from molecular precursors. (B) Synthesis of cove GNRs from molecular precursors. Schematic representation of **1**-AuNP, and **2**-AuNP composite materials is not to scale.

Step-growth polymerization of 2,7-dibromophenanthrene **3** or cyclopentadienone **4a**, followed by oxidative cyclodehydrogenation, yields structurally homogeneous samples of GNRs **1** and **2a** respectively.[49,61,65] Notably, these syntheses are scalable, and can afford grams of GNR at a time. Raman spectroscopy of **1** and **2a** shows the characteristic signatures for D, G, and radial breathing like modes (RBLM) that are consistent with the formation of extended GNRs (Supporting Information Figure S1).[47,48,66] The successful removal of trace metals (Fe, Ni) used in the bottom-up

synthesis of GNRs was confirmed by X-ray photoelectron spectroscopy (XPS) (Supporting Information Figure S2).

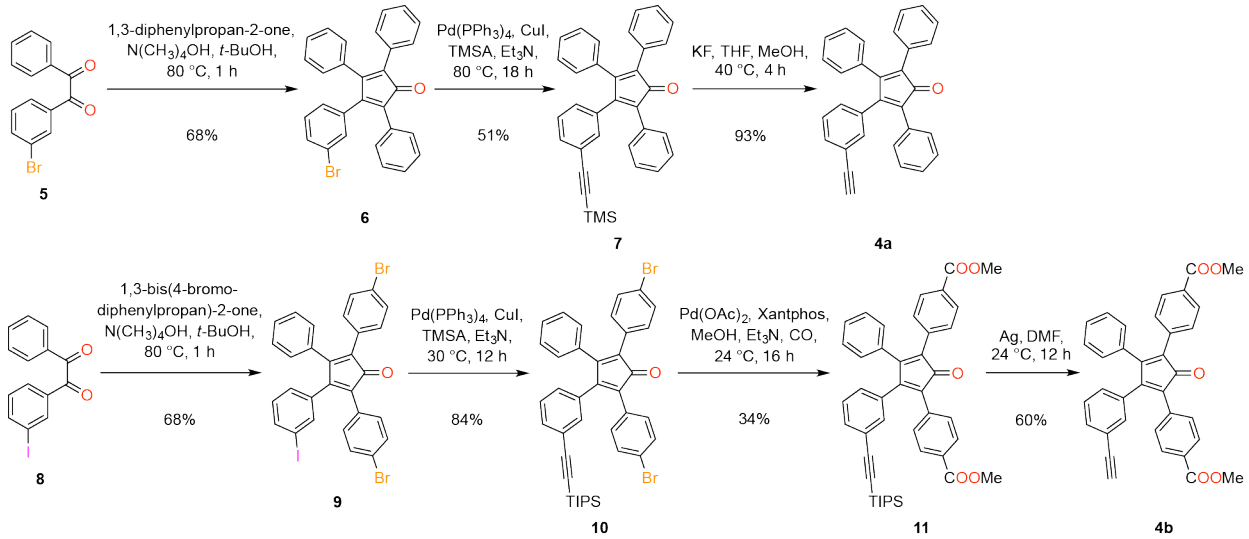

Scheme 1. Synthesis of cove-type GNR precursor monomer **4a** and ester-functionalized cove-type GNR precursor monomer **4b**.

Oleylamine-capped monodisperse AuNPs were synthesized following a procedure derived from a previously reported method.[12,67] High angle annular dark field scanning transmission electron microscopy (HAADF-STEM) of AuNPs shows the expected narrow size distribution centered around an average NP diameter of 8 nm (Figure 2A). GNR-AuNP composite materials were prepared by sonicating a dispersion of equal mass of AuNPs and the respective GNRs **1** or **2a** in hexane. The high affinity of AuNPs for the GNR support is immediately evident as the red AuNP solution loses its characteristic color upon sonication with GNRs, becoming a dark suspension. HAADF-STEM of the isolated black powder, rinsed with hexane and drop cast onto TEM grids, shows the uptake of the AuNPs into large nanoribbon aggregates (Figure 2B). GNR-AuNP composites commonly range in size from 0.2 to 1.0 μm and feature a substantial concentration of nanoparticles; STEM images of GNR samples prepared without AuNPs show aggregates of comparable size and morphology (Supporting Information Figure S3). The high density of AuNPs and the lateral overlap observed in transmission mode images suggests the AuNPs are embedded within a three dimensional GNR network, rather than perched on its surface.

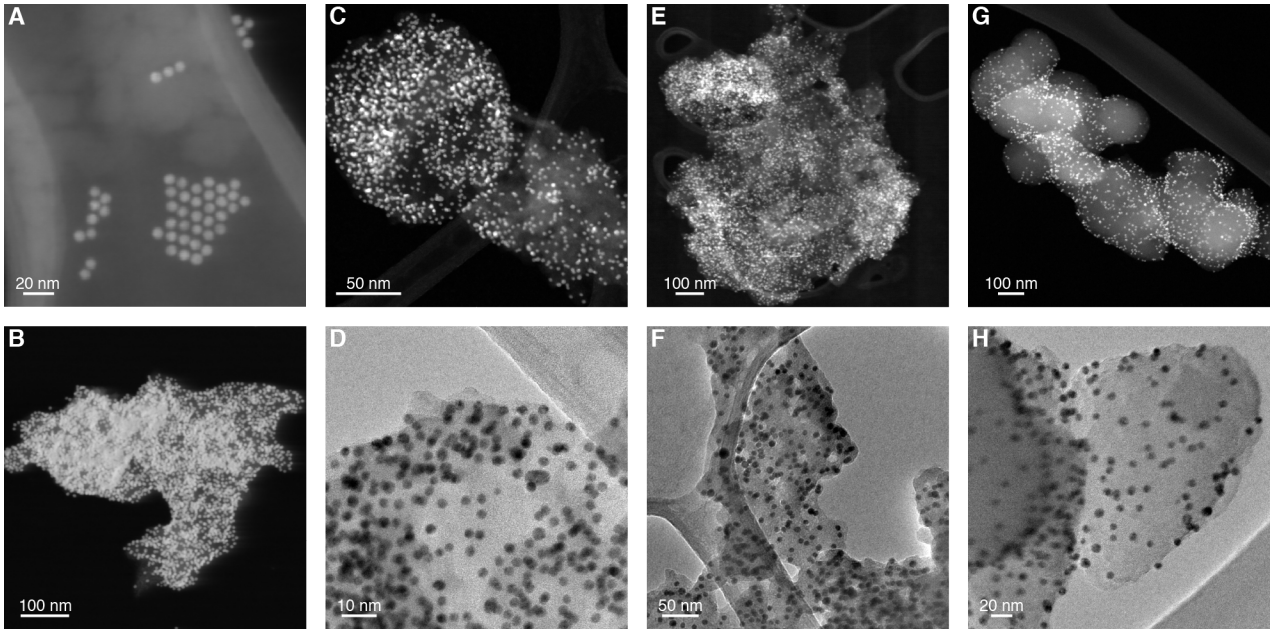

Figure 2. Electron microscopy of AuNPs and AuNP-GNR composites. (A) HAADF-STEM images of oleylamine-capped AuNPs show a narrow size distribution centered around an average NP diameter of 8 nm. (B) HAADF-STEM of unannealed **2a**-AuNP composite shows the uptake of a high density of AuNPs into the GNR aggregate. (C) HAADF-STEM and (D) TEM images of **1**-AuNP composite after annealing. (E) HAADF-STEM and (F) TEM images of **2a**-AuNP composite after annealing. (G) HAADF-STEM and (H) TEM images of **2b**-AuNP composite after annealing.

Following incorporation of AuNPs into the GNR matrix, the oleylamine capping ligands decorating the surface of AuNPs were removed by annealing GNR-AuNP composites in air at 185 °C for 10 h.[13] STEM and TEM images of annealed samples show that composite aggregates remain intact and are comparable in size and morphology to those observed prior to annealing (Figure 2C-F). IR

spectra of samples prior to and immediately after annealing confirm that the oleylamine ligands have been removed, leaving pristine AuNPs behind (Figure 3A).[67] Raman spectra of annealed GNR-AuNP composites show no shift or broadening of the diagnostic D, G, and RBLM modes (Figure 3B), indicating that the integral structure of the GNRs remains unaltered. Powder X-ray diffraction (PXRD) of the black GNR-AuNP composite shows the characteristic broadened signals of AuNPs (Figure 3C).[12,68] Although the NPs have been stripped of their stabilizing ligand shell, only minimal coalescence of the nanoparticles during the annealing process is observed by STEM, indicating an efficient stabilization of uncapped AuNPs through dispersion interactions with the GNR matrix.

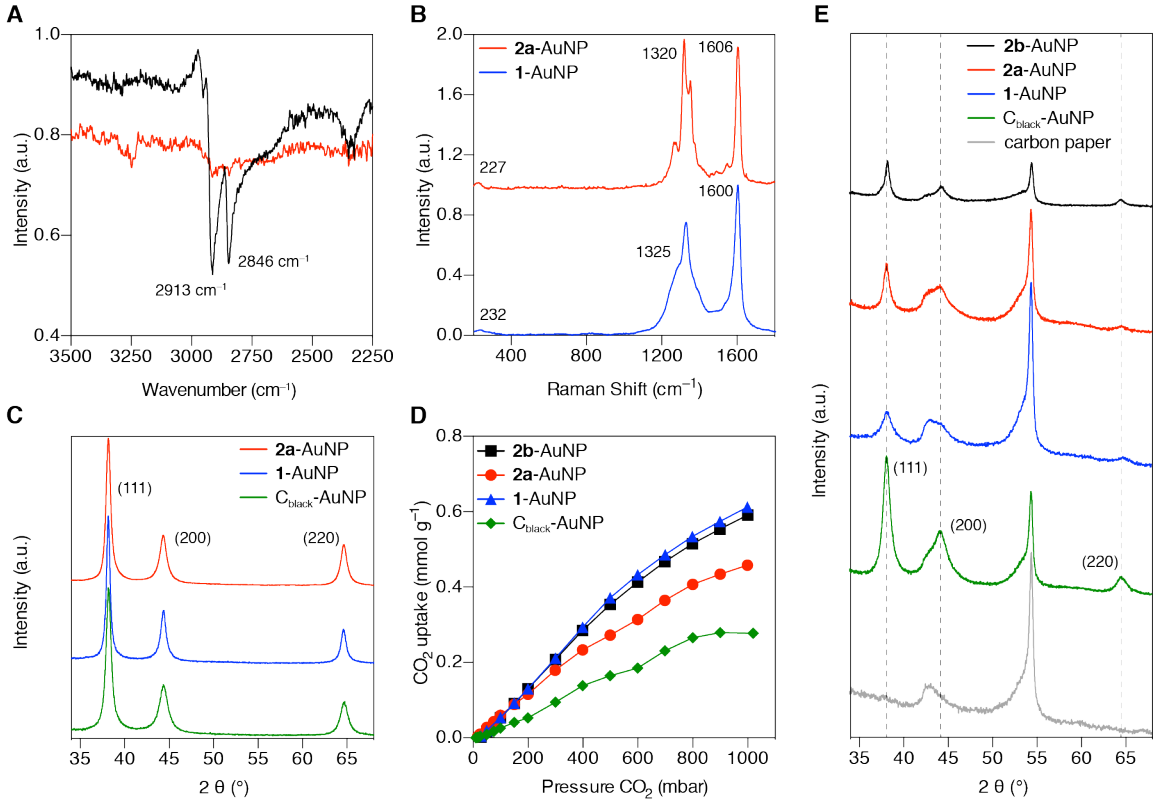

Figure 3. Characterization of AuNP-GNR composite materials. (A) IR spectroscopy of **1**-AuNP composite materials prior to (black) and after annealing (red). The characteristic vibronic signature associated with the oleylamine capping ligand is absent after the annealing at 185 °C for 10 h. (B) Raman spectra of **1**-AuNP (blue) and **2a**-AuNP (red) exhibit unaltered characteristic GNR peaks. (C) PXRD of GNR- and C_{black}-AuNP composite powders exhibit the characteristic signals of AuNPs. (D) 298 K CO_2 adsorption experiment for GNR- and C_{black}-AuNP composites. Despite having lower BET surface areas, GNR composites uptake more CO_2 than the comparable C_{black} composite, reflecting their greater microporosity. (E) PXRD of composite AuNP electrodes prepared by depositing **2b**-AuNP (black), **2a**-AuNP (red), **1**-AuNP (blue), and C_{black}-AuNP (green) on conductive carbon paper (gray) followed by annealing at 185 °C for 10 h.

Traditionally, NP support materials emphasize high surface area as a crucial factor to dynamic mass transport to and from the catalytically active surface.[69-71] However, surface area measurements derived from N_2 adsorption at 77 K (BET model, Table 1) showed that both **2a**-AuNP (5.9 $m^2\ g^{-1}$) and **1**-AuNP (19.8 $m^2\ g^{-1}$) composites present lower surface areas than a reference composite prepared from C_{black}-AuNP (26.8 $m^2\ g^{-1}$). This behavior is not unexpected in aggregates of a graphitic material, for which strong dispersion interactions between graphene planes lead to stacking and low BET surface area.[72] Furthermore, it has been shown that N_2 adsorption at 77 K does not appreciably capture ultramicroporosity (pore size < 0.7 nm) due to restricted diffusion of N_2 into micropores at low temperature.[73-77] CO_2 absorption at 298 K is not restricted by micropore diffusion and provides a better approximation for the transport of small gas molecules through the GNR matrix.[78,79] AuNP composites of **1** and **2a** show more than twice the CO_2 uptake measured for the C_{black}-AuNP reference (Figure 3D), reversing the trend in BET surface area observed for N_2 adsorption. These results suggest a significant microporosity for the GNR aggregates in comparison to the C_{black} composite, and is an indication that GNRs, despite their inherently low surface area, can facilitate mass transport within NP composite aggregates.

We determined the electrochemically active surface area (ECSA) of AuNP composites using lead underpotential deposition experiments (Pb-UPD) (Figure 4A, Table 1).[15,67,80,81] All samples display two characteristic signals in the Pb-UPD voltammograms, corresponding to lead deposition on the Au(111) and Au(110) faces, respectively. Integration of the peaks in comparison to an Au foil standard provides a quantitative measure of the accessible surface area of the AuNPs. Electrodes fabricated from GNR-AuNP composites have greater ECSA (2.87 and 4.60 cm^2/mg AuNP for **1**- and **2a**-AuNP composites, respectively) than the corresponding C_{black}-AuNP reference (1.70 cm^2/mg AuNP) at the same nanoparticle loading. ECSA is a direct quantitative measure for the ability of a support material to disperse and immobilize nanoparticles without obstructing the transport of reactants and products to and from

the nanoparticle surface.[29-30,43-44] The significantly higher ECSA measured for GNR-AuNP composites indicates that GNRs, and in particular GNR **2a**, facilitate the dispersion of AuNPs and do not obstruct access to the catalytically active metal surface.

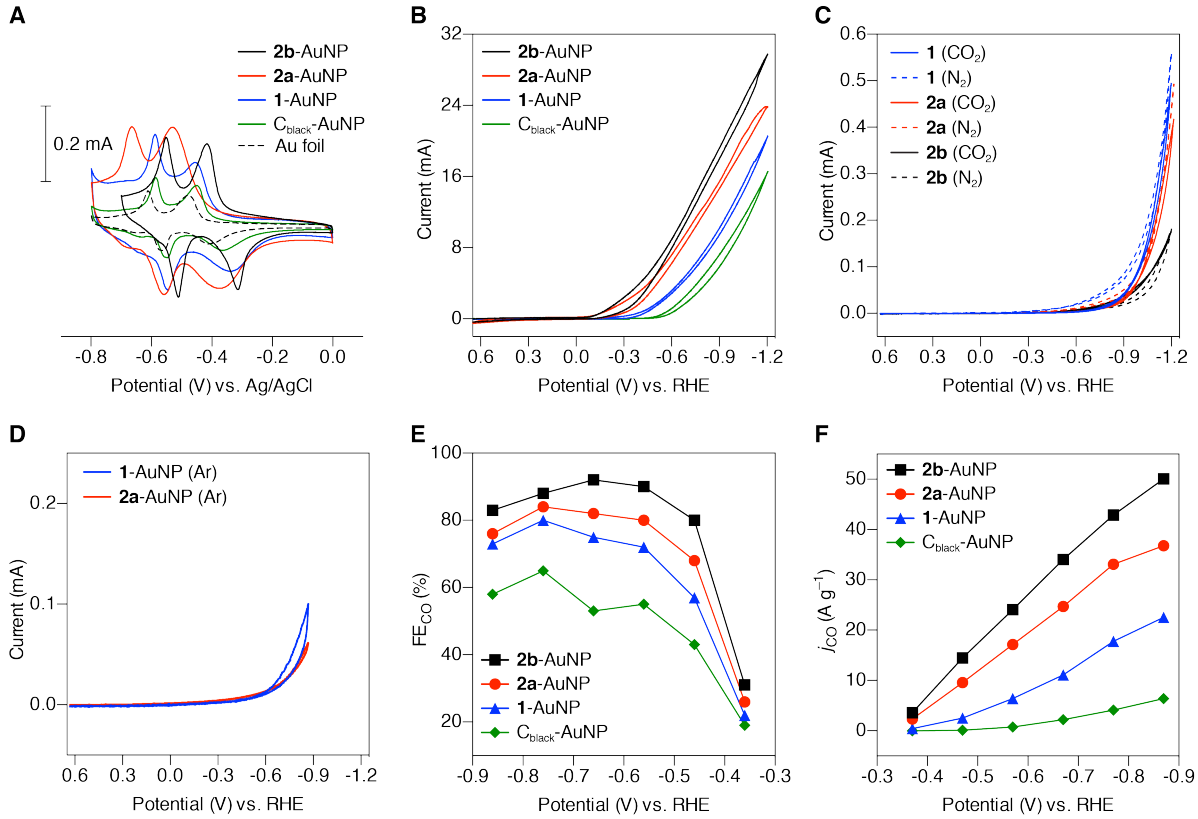

Figure 4. (A) Lead underpotential deposition experiments to determine the AuNP electrochemically active surface area (ECSA) of AuNP composite electrodes. Pb-UPD experiments for **1**-AuNP composite electrodes (blue), **2a**-AuNP composite electrodes (red), and **2b**-AuNP composite electrodes (black) indicate much higher ECSA for the GNR composites than for C_{black}-AuNP composite electrodes (green). The active surface area was determined based on a reference Au foil electrode (black). (B) Cyclic voltammograms of **1**-AuNP (blue), **2a**-AuNP (red), and **2b**-AuNP (black) composite materials in 0.5 M aqueous $KHCO_3$ saturated with CO_2 (pH 7.3). The performance of C_{black}-AuNP (green) serves as a standard reference. (C) Cyclic voltammograms of **1** (blue), **2a** (red), and **2b** (black) electrodes, prepared without AuNPs, in 0.5 M aqueous $KHCO_3$ (pH 7.3) saturated with CO_2 (full lines) and N_2 (dotted lines). (D) Cyclic voltammograms of **1**-AuNP composite electrodes (blue) and **2a**-AuNP composite electrodes (red) in 0.5 M aqueous KHCO3 (pH 7.3) saturated with Ar. (E) Faradaic efficiencies for CO production (FE_{CO}) by **1**-AuNP (blue triangles), **2a**-AuNP (red circles), **2b**-AuNP (black squares) and C_{black}-AuNP (green diamonds) composite electrodes. Electrolysis performed at potentials from –0.37 V to –0.87 V vs RHE in 0.5 M aqueous $KHCO_3$ saturated with CO_2 (pH 7.3). (F) Partial current for CO production (j_{CO}) by **1**-AuNP (blue triangles), **2a**-AuNP (red circles), **2b**-AuNP (black squares) and C_{black}-AuNP (green diamonds) composite electrodes. Electrolysis performed at regular potentials from –0.37 V to –0.87 V vs RHE in 0.5 M aqueous $KHCO_3$ saturated with CO_2 (pH 7.3).

In an effort to benchmark the performance of GNR-AuNP composite materials with respect to traditional supports like C_{black},[13] we studied the electrocatalytic reduction of CO_2 in aqueous $KHCO_3$ buffered solution. AuNP composites with single-walled carbon nanotubes (SWCNTs) were examined as a second point of reference, but the comparatively poor performance of the SWCNT composites made them an unsuitable standard (Supporting Information Figure S4). GNR-AuNP composite electrodes were fabricated by drop casting a sonicated dispersion of AuNPs and the respective GNRs (1:1 by mass with either **1** or **2a**; composites made using GNR **2b** are discussed later) in hexane onto conductive carbon paper, followed by thermal annealing in air at 185 °C for 10 h. The characteristic PXRD pattern of AuNPs in these annealed electrodes matches that of the composite bulk powders characterized above (Figure 3E). Cyclic voltammetry of the resulting composite electrodes (Figure 4B) in 0.5 M aqueous $KHCO_3$ saturated with CO_2 (pH 7.3) reveals a strong synergistic effect between nanoparticles and GNRs. Composite electrodes formed from GNRs **1** or **2a** and AuNPs deliver significantly more current than corresponding electrodes made from AuNPs alone, or AuNPs supported by a C_{black} matrix. Notably, electrodes fabricated from GNRs without any added AuNPs produce minimal current across the entire examined potential window (Figure 4C), indicating that the GNRs themselves are not electrochemically active. The current enhancement observed in GNR-AuNP composite electrodes disappears in the absence of CO_2 (Figure 4D), suggesting the excess current drives CO_2 reduction.

When compared to a C_{black}-AuNP reference, GNR composites exhibit a catalytic onset (defined here as the potential at which current density exceeds 0.5 mA cm^{-2}) at significantly positively shifted potentials (–0.36 V for **1**- and –0.14 V for **2a**-AuNP composites, versus –0.54 V for C_{black}-AuNP, all potentials vs. reversible hydrogen electrode (RHE), Table 1), indicating the catalytic environment created by the GNR support significantly lowers the required overpotential for CO_2 reduction on AuNPs. This shift in catalytic onset is consistent with the formation of a Mott-Schottky heterojunction at the GNR-AuNP interface.[52,53,56-58] Lower work function materials promote charge migration across the semicon-

ductor-NP interface towards the high work function AuNPs, increasing electron density at the metal surface and shifting the catalytic onset.[31,42,44-45,82-87] Theory and experiment indicate that the semiconducting GNRs employed here, and particularly cove-type GNRs, feature appreciably lower work functions than other carbon supports like graphene or C_{black}, consistent with the positively shifted onset potentials observed (Table 1).[37,46-47,86,88-92]

Table 1. Physical and electrocatalytic characterization of AuNP composites.

	BET Surface Area ($m^2\ g^{-1}$)[a]	AuNP Electrochemically Active SA ($cm^2\ mg^{-1}$ AuNP)[b]	Onset Potential (mV vs RHE)[c]	CO_2 reduction activity[d] j_{CO} ($A\ g^{-1}$)	ECSA-normalized CO_2 reduction activity[d] j_{CO} ($mA\ cm^{-2}$)
1-AuNP	19.8	2.87	–0.36	22.6	7.87
2a-AuNP	5.9	4.60	–0.14	36.8	8.00
C_{black}-AuNP	26.8	1.70	–0.54	6.4	3.76

[a] Measured by N_2 sorption at 77 K; [b] Measured by lead underpotential deposition; [c] Potential at which total CV activity exceeded 0.5 mA cm^{-2}, measured in 0.5 M aqueous $KHCO_3$ saturated with CO_2 (pH 7.3); [d] Total CV activity at –0.87 V vs RHE, measured in 0.5 M aqueous $KHCO_3$ saturated with CO_2 (pH 7.3).

One hour controlled potential electrolysis experiments over a potential range from –0.87 V to –0.37 V underline the synergy between AuNPs and GNRs. Both Faraday efficiency (FE_{CO}, Figure 4E) and partial current (j_{CO}, Figure 4F) for CO_2 reduction to CO by GNR-AuNP composites dramatically exceed those of C_{black}-AuNP across a broad potential window. Selectivity in particular was starkly improved for GNR composites, with increased j_{CO} leading to FE_{CO} values exceeding 80%, as much as 29 percentage points higher than those of C_{black}-AuNP composites across the entire potential window. **2a**-AuNP composites deliver the highest activity and selectivity, consistent with a larger ECSA and lower CO_2 reduction onset potential. Notably, at potentials distant from their catalytic onsets the activity of GNR composites is closely proportional to their measured ECSAs (Table 1). While GNR-AuNP composites do not suppress hydrogen evolution, as the partial current for proton reduction (j_{H2}) is comparable to C_{black}-AuNP composites (Supporting Information Tables S1–S4), the observed increase in selectivity reflects a greatly enhanced activity of GNR-AuNPs towards CO_2 reduction.

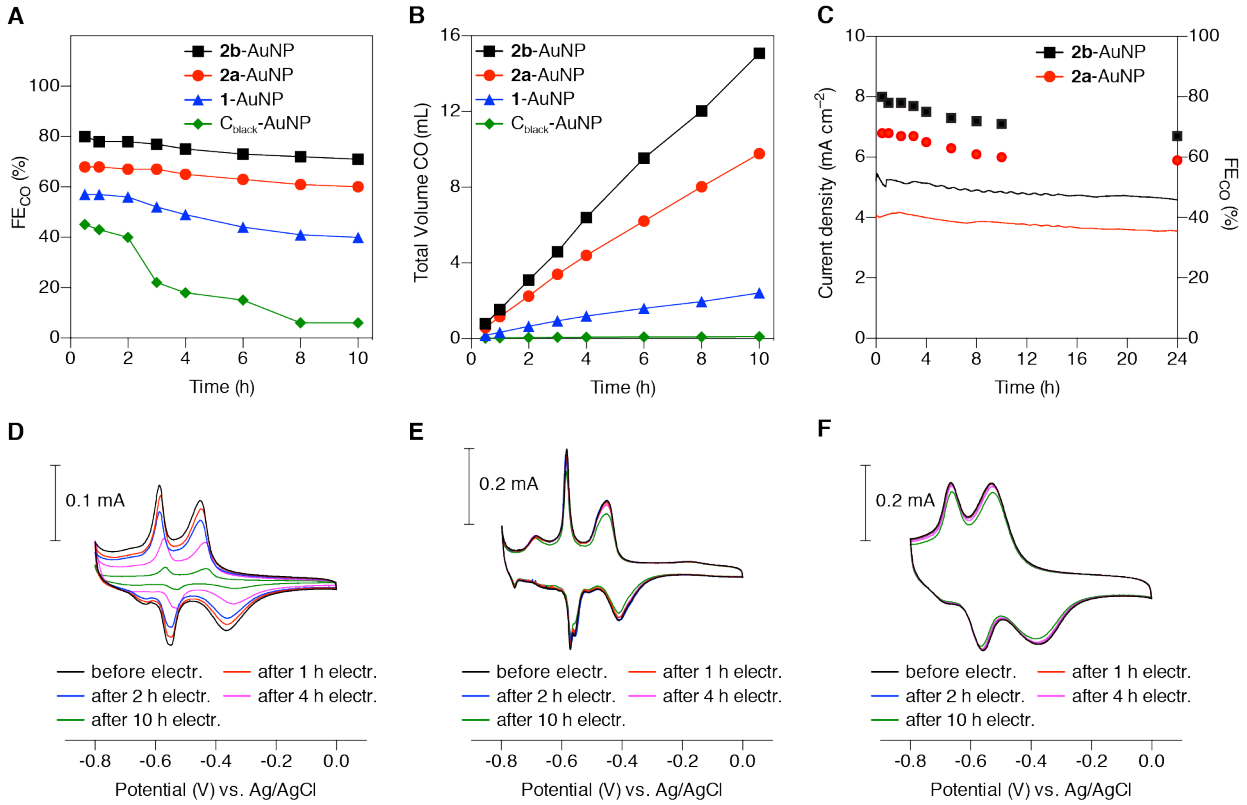

Figure 5. (A) Faraday efficiencies for CO production (FE_{CO}) by **1**-AuNP (blue triangles), **2a**-AuNP (red circles), **2b**-AuNP (black squares) and C_{black}-AuNP (green diamonds) composite electrodes. Electrolysis performed in 0.5 M aqueous $KHCO_3$ saturated with CO_2 (pH 7.3). (B) Total volume (at STP) of CO produced by **1**-AuNP (blue triangles), **2a**-AuNP (red circles), **2b**-AuNP (black squares) and C_{black}-AuNP (green diamonds) composite electrodes. Electrolysis performed in 0.5 M aqueous $KHCO_3$ saturated with CO_2 (pH 7.3). (C) Total current density for **2a**-AuNP (red line) and **2b**-AuNP (black line) over 24 h. Faraday efficiency for CO production with **2a**-AuNP (red circles) and **2b**-AuNP (black squares) over 24 h. Both current density and Faraday efficiency show little change between 10 and 24 h of fixed potential electrolysis at –0.47 V vs RHE. (D–F) Cyclic voltammograms for lead underpotential deposition experiments on AuNP composite electrodes following extended controlled-potential electrolysis

at –0.47 V vs RHE, to measure the change in AuNP ECSA. Cyclic voltammetry was performed in 0.1 M aqueous KOH containing 1 mM $Pb(OAc)_2$ and purged with Ar. C_{black}-AuNP composite electrodes (D) exhibit significant decline in ECSA following fixed potential electrolysis experiments. **1**-AuNP composites (E) and **2a**-AuNP composites (F) retain almost all of their ECSA following fixed potential electrolysis experiments.

We performed bulk electrolysis experiments to evaluate the ability of GNRs to stabilize AuNPs over extended reaction times (Figure 5A). AuNPs supported by C_{black} degrade rapidly, delivering only 22% FE_{CO} after 3 h. Electrodes instead fabricated from GNR-AuNP composites maintain superior performance for more than 10 h of continuous electrolysis. At –0.47 V, **2a**-GNR composites retained 88% of their original FE_{CO} after 10 h of catalysis, and produced more than 33 mL CO per mg of AuNP, compared with only 0.4 mL CO per mg AuNP for the C_{black} composite electrodes prepared from the same AuNPs (Figure 5B). Longer controlled-potential experiments indicated that the **2a**-AuNP composite in particular had reached a plateau of stability; over 24 h of uninterrupted catalysis at –0.47 V, the composite delivered 87% of its original FE_{CO}, nearly unchanged from the 10 h experiment (Figure 5C).

We interrogated the origin of nanoparticle stabilization in GNR-AuNP composites. Pb-UPD experiments at selected time points during bulk electrolysis reveal the change in the ECSA of the AuNPs. During the electrolysis with C_{black}-AuNP composites (–0.47 V), a significant reduction in active Au surface area, that correlates with the loss of catalytic activity, can be observed within hours (Figure 5D). After 4 h of catalysis, only 48% of the original Au surface area remains, and only 15% is retained after 10 h. TEM images of C_{black}-AuNP composites recorded following 3 h of bulk electrolysis suggest that a plausible mechanism of deactivation relies on the coalescence of AuNPs to form larger aggregates with significantly reduced active surface area (Supporting Information Figure S5).[24] **1**-AuNP (Figure 5E) and **2a**-AuNP (Figure 5F) composites effectively prevent NP coalescence and the associated reduction in ECSA. **2a**-AuNP composites in particular lose only 4% of their active Au surface area over 4 h of catalysis (10% over 10 h). We suggest that the effective immobilization of the NPs through strong dispersion interactions with the matrix of narrow, flexible GNRs effectively precludes NP mobility and prevents coalescence into larger structures.

A unique advantage of bottom-up synthesized GNRs as functional nanoparticle supports, unmatched by other graphitic support materials, lies in their inherent molecular-level tunability. The rational synthesis from small-molecule precursors provides an absolute control over key functional parameters such as shape, dimension, and electronic structure, and enables the deterministic introduction of functional groups. GNR **2b**, a cove-type GNR bearing methyl carboxylate groups along its edges, was synthesized from the ester functionalized cyclopentadienone **4b** (Scheme 1). Raman spectroscopy of **2b** shows characteristic peaks for the D, G, and RBLM peaks reminiscent of the unsubstituted **2a**, while IR spectroscopy confirms the presence of methyl carboxylate groups in the fully cyclized GNR (Supporting Information Figure S6).

AuNP composites prepared from the ester-modified **2b** resembled those of **2a** by STEM and TEM (Figure 2G,H), and displayed a similar low surface area (12.6 $m^2\ g^{-1}$) and CO_2 uptake behavior at 298 K (Figure 3D). The ECSA of **2b**-AuNP as measured by Pb-UPD (4.4 cm^2/mg AuNP) was very similar to that of the parent **2a**-AuNP composite (Figure 4A). The electrocatalytic performance of **2b**-AuNP composites, however, was found to be strikingly different from that of the unfunctionalized composite (Figure 4E,F). A significantly increased CO_2 reduction activity is reflected in both an increased j_{CO} and a higher FE_{CO}, and can only be attributed to the functionalization of the GNR support. A 1 h controlled potential experiment at –0.66 V revealed a 92% FE_{CO} for the **2b**-AuNP composite, a remarkable improvement over the 53% FE_{CO} observed for the C_{black}-AuNP composite under the same conditions. In comparison to composites of the unfunctionalized GNR **2a**, the rate of hydrogen production is nearly unchanged, but FE_{CO} is improved across the potential window owing to an approximately 50% increase in the rate of CO production (Supporting Information Tables S1–S4).

The improved performance is retained throughout long-term experiments; for a 10 h experiment at –0.47 V, **2b**-AuNP electrodes deliver an overall FE_{CO} of 71%, retaining 91% of the FE_{CO} performance (78%) exhibited in the first hour at that potential (Figure 5A). A 24 h experiment at the same potential delivered a total FE_{CO} of 67% (86% of the FE_{CO} recorded for the first hour), with the composite's characteristic increased activity remaining nearly constant for the duration (Figure 5C). Over the course of 10 h, the ester-functionalized composite produced more than 50 mL of CO per mg AuNP, representing a 137-fold increase in total catalytic output over the same nanoparticles embedded in a C_{black} matrix (Figure 5B). The overall efficiency performance of **2b** composite after 10 hours of electrocatalysis is comparable to the first hour of composite **2a**, and exceeds the initial performance of any other material tested.

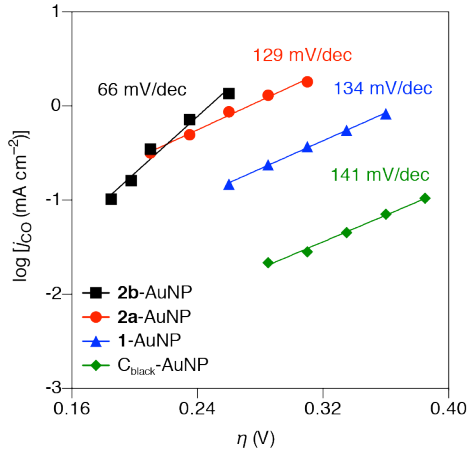

Figure 6. Tafel study of CO_2 reduction by GNR- and C_{black}-AuNP composite materials. A Tafel analysis shows the CO_2 reduction behavior of AuNP composites with **1** (blue triangles) and **2a** (red circles). Tafel slopes are comparable to that of the C_{black} (green diamonds) composite, indicating no shift in the mechanism of CO_2 reduction for those materials. For the **2b**-AuNP composite (black squares), however, the Tafel slope is markedly different, indicating that the catalytic environment created by the support material changed the mechanism of CO_2 reduction at the AuNP surface.

To better understand the source of the marked increase in performance exhibited by **2b**-AuNP composites, the kinetics of CO_2 reduction for each composite were studied using Tafel analysis. Figure 6 shows that the functionalization of cove GNRs with methyl carboxylates alters the mechanistic pathway for CO_2 reduction at the Au nanoparticle surface. A Tafel slope of 141 mV/decade for C_{black}-AuNP is consistent with the expected value for a rate-limiting

single-electron transfer to adsorbed CO_2 to generate the radical anion.[23,90,91] This observation and proposed mechanism conform with previous studies of aqueous CO_2 reduction by AuNPs.[23,67] Composites made from both GNRs **1** and **2a**, although delivering greater overall current, exhibit similar Tafel slopes to that of the C_{black} composite, indicating that the mechanism for CO_2 reduction is unchanged for these materials. In contrast, the Tafel slope for the composite made with GNR **2b** is only 66 mV/decade, suggesting a change in the rate-limiting step, and thus a significant change in the overall electrocatalytic mechanism. The Tafel slope observed for the ester functionalized GNR-AuNP composite is consistent with a pre-equilibrating one-electron transfer followed by a rate-limiting chemical step.[8,93,94] These data suggest that an interaction between the reactant and the introduced methyl carboxylates stabilizes the transition state of the erstwhile rate-limiting electron-transfer step, thereby changing the mechanism and leading to the increased activity observed for this composite. This experiment serves as primary evidence that nanoparticle electrocatalysis is responsive to the immediate catalytic environment created by the support material, and supports the assertion that the chemical tunability of a bottom-up synthesized support material can greatly improve catalytic performance.

CONCLUSION

Through the greatly enhanced CO_2 reduction performance of electrocatalytic AuNPs, we have demonstrated that narrow, bottom-up synthesized GNRs excel as functional catalyst support materials. The catalytic environment created by GNR-NP interaction led to reduced onset potential and high activity, with excellent nanoparticle dispersion reflected in a greatly increased ECSA. Electrocatalytic stability was markedly improved for GNR composites, yielding consistent catalytic performance and stable ECSA over periods as long as 24 h. Furthermore, the bottom-up synthetic approach to these materials imparts an unrivaled ability to precisely tune the catalytic environment, demonstrated by the marked increase in performance and change in mechanism following the synthetic functionalization of a GNR support. Our findings have implications across the wide range of fields and applications that make use of inorganic nanoparticles, for which GNRs could prove a powerful complement.

EXPERIMENTAL METHODS

Nanoparticle Synthesis. Au nanoparticles were synthesized by a procedure derived from literature reports.[12,27] A 50 mL Schlenk flask was charged under Ar with 1-octadecene (10 mL) and heated to 125 °C for 30 min with stirring. The reaction was cooled to 24 °C and oleic acid (0.32 mL, 283 mg, 1.0 mmol), oleylamine (0.33 mL, 268 mg, 1.0 mmol), chloroauric acid trihydrate (118 mg, 0.3 mmol), and 1,2-hexadecanediol (517 mg, 2mmol) were added. The mixture was heated under Ar to 210 °C and stirred for 3 h before cooling to 24 °C. The product was precipitated by addition of a mixture of EtOH (2 mL) and acetone (8 mL) and collected by centrifugation (7500 rpm, 8 min). The collected solid was dried under vacuum to yield AuNPs as a gold-colored solid (32 mg). AuNPs were redispersed in hexane (2 mg mL^{-1}) prior to use.

Preparation of GNR-AuNP Composite Materials. A 3 mL vial was charged with GNRs (0.3 mg) and AuNPs (0.3 mg) in hexane (1 mL). The mixture was sonicated for 1 h. The precipitate was collected by vacuum filtration, washed thoroughly with hexane, and dried under vacuum. The solid was annealed in air for 10 h at 185 °C to yield GNR-AuNP composite as a black a powder.

Preparation of GNR-AuNP Composite Samples for TEM. Samples of GNR-AuNP composite for TEM were prepared following the general synthesis above. Prior to annealing the precipitate, it was resuspended in hexane (1 mL) and sonicated for 1 h. The suspension was dropcast on the copper face of a Ted Pella 01824 grid (ultrathin carbon film on lacey carbon, 400 mesh Cu), and promptly wicked away from the opposite side with a laboratory wipe. The grid was annealed in air for 10 h at 185 °C and stored under vacuum prior to imaging.

Preparation of AuNP Composite Working Electrodes. A 3 mL vial was charged with the appropriate carbon support material (GNRs or C_{black}, 0.3 mg) and AuNPs (0.3 mg) in hexane (1 mL). The mixture was sonicated for 1 h. The resulting suspension was dropcast onto a 1 cm^2 area of carbon paper (TGP-H-060 Toray). The carbon paper was annealed in air for 10 h at 185 °C prior to contacting with silver wire.

Electrochemical Measurements. All electrochemical experiments were performed in a custom three-piece glass electrochemical cell, including a working compartment body, a working compartment lid, and a counter compartment body. An anion exchange membrane (Selemion AMV) separates the working and counter electrode (Pt wire) compartments (200 mL). The body of the working compartment was charged with a 3 cm long Teflon-coated stir bar and 150 mL of electrolyte solution (0.5 M aqueous $KHCO_3$), and the lid was fitted with a composite working electrode and a Ag/AgCl reference electrode. The counter compartment was filled with 50 mL of electrolyte solution, and equipped with a Teflon cap with a septum, as well as a graphite auxiliary electrode. The electrolyte solution in the working compartment was sparged for 20 min with CO_2. 1 mL ethylene was then injected into the headspace as the internal standard for GC analysis. Electrolysis was performed at a constant potential. The headspace of the cell was analyzed by GC. Cyclic voltammetry was performed at a scan rate of 50 mV s^{-1} using the same electrochemical setup, following 20 min electrolysis at –1.30 V vs. Ag/AgCl. Multiple working electrodes prepared for each GNR composite sample showed consistent current output. Gaseous products CO and H_2 were quantified by gas chromatography (GC), and no liquid products were detected by ^{1}H-NMR, in accordance with the reported behavior of AuNP in CO_2 reduction.[13,21,22] Additional details are provided in the Supporting Information.

Lead Underpotential Deposition. The electrochemically active surface area of working electrodes was determined by measuring the charge associated with the stripping of an underpotential deposited (upd) Pb monolayer. The electrodes were immersed in an aqueous KOH (0.1 M) solution containing $Pb(OAc)_2$ (1 mM) purged with Ar in a two-compartment electrochemical cell (Pt gauze counter electrode, Ag/AgCl (3 M KCl) reference electrode). Cyclic voltammagrams from 0.0–0.8 V with a scan rate of 50 mV s^{-1} were acquired until traces converged. The anodic stripping wave associated with the Au(110) surface was integrated and normalized by comparison to a reference Au foil (0.64 cm^2).

ASSOCIATED CONTENT

Supporting Information

The Supporting Information is available free of charge on the ACS Publications website.

Synthesis and characterization of materials, Figure S1–S20, and Table S1–S4 (PDF).

AUTHOR INFORMATION

Corresponding Author

*E-mail: ffischer@berkeley.edu

Notes

The authors declare no competing financial interest.

ACKNOWLEDGMENT

Research supported by the U.S. Department of Energy (DOE), Office of Science, Basic Energy Science (BES), under Award # DE-SC0010409; TEM and STEM imaging performed at the Molecular

Foundry was supported by the Office of Science, Office of Basic Energy Sciences, of the U.S. Department of Energy under Contract No. DE-AC02-05CH11231; Berkeley NMR Facility is supported in part by NIH grant SRR023679A; Berkeley X-ray Facility is supported in part by NIH Shared Instrumentation Grant S10-RR027172.

REFERENCES

(1) Raimondi F.; Scherer G. G.; Kotz R.; Wokaun A. *Angew. Chem. Int. Ed.* **2005**, *44*, 2190–2209.

(2) Guo Y.-G.; Hu J.-S.; Wan L.-J. *Adv. Mater.* **2008**, *20*, 2878–2887.

(3) Galvis H. M.; Bitter J. H. ; Khare C. B.; Ruitenbeek M.; Dugulan A. I.; de Jong K. P. *Science* **2012**, *17*, 835–838.

(4) Chen C.; Kang Y.; Huo Z.; Zhu Z.; Huang W.; Xin H. L.; Snyder J. D.; Li D.; Herron J. A.; Mavrikakis M.; Chi M.; More K. L.; Li Y.; Markovic N. M.; Somorjai G. A.; Yang P.; Stamenkovic V. R. *Science* **2014**, *21*, 1339–1343.

(5) Kim D.; Sakimoto K. K.; Hong D.; Yang P. *Angew. Chem. Int. Ed.* **2015**, *54*, 3259–3266.

(6) Whipple D. T.; Kenis P. J. A. *J. Phys. Chem. Lett.* **2010**, *1*, 3451–3458.

(7) Coq B.; Figueras F. *Coord. Chem. Rev.* **1998**, *178–180*, 1753–1783.

(8) Chen Y.; Li C. W.; Kanan M. W. *J. Am. Chem. Soc.* **2012**, *134*, 19969–19972.

(9) Reske R.; Mistry H.; Behafarid F.; Cuenya B. R.; Strasser P. *J. Am. Chem. Soc.* **2014**, *136*, 6978–6986.

(10) Mistry H.; Reske R.; Zeng Z.; Zhao Z.-J.; Greeley J.; Strasser P.; Cuenya B. R. *J. Am. Chem. Soc.* **2014**, *136*, 16473–16476.

(11) Zhu W.; Zhang Y.-J.; Zhang H.; Lv H.; Li Q.; Michalsky R.; Peterson A. A.; Sun S. *J. Am. Chem. Soc.* **2014**, *136*, 16132–16135.

(12) Kim D.; Resasco J.; Yu Y.; Asiri A. M.; Yang P. *Nat. Commun.* **2014**, *5*, 4948.

(13) Zhu W.; Michalsky R.; Metin Ö.; Lv H.; Guo S.; Wright C. J.; Sun X.; Peterson A. A.; Sun S. *J. Am. Chem. Soc.* **2013**, *135*, 16833–16836.

(14) Gao D.; Zhou H.; Wang J.; Miao S.; Yang F.; Wang G.; Wang J.; Bao X. *J. Am. Chem. Soc.* **2015**, *137*, 4288–4291.

(15) Feng X.; Jiang K.; Fan S.; Kanan M. W. *J. Am. Chem. Soc.* **2015**, *137*, 4606–4609.

(16) Hall A. S.; Yoon Y.; Wuttig A.; Surendranath Y. *J. Am. Chem. Soc.* **2015**, *137*, 14834–14737.

(17) Liu M.; Pang Y.; Zhang B.; De Luna P.; Voznyy O.; Xu J.; Zheng X.; Dinh C. T.; Fan F.; Cao C.; Pelayo García de Arquer F.; Safaei T. S.; Mepham A.; Klinkova A.; Kumacheva E.; Filleter T.; Sinton D.; Kelley S. O.; Sargent E. H. *Nature* **2016**, *537*, 382–386.

(18) Ertl G. *Angew. Chem. Int. Ed.* **1990**, *29*, 1219–1227.

(19) Somorjai G. A. *Surf. Sci.* **1994**, *299–300*, 849–866.

(20) Zhang S.; Nguyen L.; Zhu Y.; Zhan S.; Tsung C.-K.; Tao F. *Acc. Chem. Res.* **2013**, *46*, 1731–1739.

(21) Hori Y.; Murata A.; Kikuchi K.; Suzuki S. *J. Chem. Soc. Chem. Commun.* **1987**, *10*, 728–729.

(22) Hori Y.; Wakebe H.; Tsukamoto T.; Koga O. *Electrochim. Acta* **1994**, *39*, 1833–1839.

(23) Koh J. H.; Jeon H. S.; Jee M. S.; Nursanto E. B.; Lee H.; Hwang Y. J.; Min B. K. *J. Phys. Chem. C.* **2015**, *119*, 883–889.

(24) Manthiram K.; Surendranath Y.; Alivisatos A. P. *J. Am. Chem. Soc.* **2014**, *136*, 7237–7240.

(25) Zhou X.; Qiao J.; Yang L.; Zhang J. *Adv. Energy Mater.* **2014**, *4*, 1301523.

(26) Fujigaya T.; Kim C.; Hamasaki, Y.; Nakashima, N. *Sci. Rep.* **2016**, *6*, 21314.

(27) Yin H.; Tang H.; Wang D.; Gao Y.; Tang Z. *ACS Nano* **2012**, *6*, 8288-8297.

(28) Shao Y.; Yin G.; Gao Y. *J. Power Sources* **2007**, *171*, 558-566.

(29) Shao Y.; Yin G.; Gao Y.; Shi P. *J. Electrochem. Soc.* **2006**, *153*, A1093-A1097.

(30) Wang X.; Tan Z.; Zeng M.; Wang J. *Sci. Rep.* **2014**, *4*, 4437.

(31) Ding M.; Tang Y.; Star A. *J. Phys. Chem. Lett.* **2013**, *4*, 147-160.

(32) Navalon S.; Dhakshinamoorthy A.; Alvaro M.; Garcia H. *Coord.Chem. Rev.* **2016**, *312*, 99-148.

(33) Liu M.; Zhang R.; Chen W. *Chem. Rev.* **2014**, *114*, 5117-5160.

(34) Zhang S.; Shao Y.; Liao H.; Liu J.; Aksay I.; Yin G.; Lin Y. *Chem. Mater.* **2011**, *23*, 1079-1081.

(35) Gracia-Espino E.; Hu G.; Shchukarev A.; Wågberg T. *J. Am. Chem. Soc.* **2014**, *136*, 6626-6633.

(36) Zhou J.; Zhou X.; Sun W.; Li R.; Murphy M.; Ding Z.; Sun X.; Sham T. *Chem. Phys. Lett.* **2007**, *437*, 229-232.

(37) Khomyakov P.; Giovannetti G.; Rusu P.; Brocks G.; van den Brink J.; Kelly P. *Phys. Rev. B* **2009**, *79*, 195425.

(38) Coloma F.; Sepúlveda-Escribano A.; Rodríguez-Reinoso F. *J. Catalysis* **1995**, *154*, 299-305.

(39) Chambers A.; Nemes T.; Rodriguez N.; Baker R. T. *J. Phys. Chem. B* **1998**, *102*, 2251-2258.

(40) Truong-Phuoc L.; Pham-Huu C.; Da Costa V.; Janowska I. *Chem. Commun.* **2014**, *50*, 14433-14435.

(41) Wei W.; Wang G.; Yang S.; Feng X.; Müllen K. *J. Am. Chem. Soc.* **2015**, *137*, 5576-5581.

(42) Khoa N.; Kim S.; Yoo D.; Kim E.; Hahn S. *Appl. Catal., A* **2014**, *469*, 159-164.

(43) Li Y.; Gao W.; Ci L.; Wang C.; Ajayan P. *Carbon* **2010**, *48*, 1124-1130.

(44) Girishkumar G.; Hall T.; Vinodgopal, K.; Kamat, P. *J. Phys. Chem. B* **2006**, *110*, 107-114.

(45) Jeong G.; Suzuki S.; Kobayashi Y. *Nanotechnology* **2009**, *20*, 285708.

(46) Lee W.; Maiti U.; Lee J.; Lim J.; Han T.; Kim S. *Chem. Commun.* **2014**, *50*, 6818-6830.

(47) Vo T. H.; Shekhirev M.; Kunkel D. A.; Morton M. D.; Berglund E.; Kong L.; Wilson P. M.; Dowben P. A.; Enders A.; Sinitskii A. *Nat. Commun.* **2014**, *5*, 3189.

(48) Narita A.; Feng X.; Hernandez Y.; Jensen S. A.; Bonn M.; Yang H.; Verzhbitskiy I. A.; Casiraghi C.; Hansen M. R.; Koch A. H.; Fytas G.; Ivasenko O.; Li B.; Mali K. S.; Balandina T.; Mahesh S.; De Feyter S.; Müllen K. *Nat. Chem.* **2014**, *6*, 126–132.

(49) Müllen K. *ACS Nano* **2014**, *8*, 6531-6541.

(50) Narita A.; Verzhbitskiy I.; Frederickx W.; Mali K.; Jensen S.; Hansen M.; Bonn M.; De Feyter S.; Casiraghi C.; Feng X.; Müllen K. *ACS Nano* **2014**, *8*, 11622-11630

(51) Narita A.; Feng X.; Müllen K. *Chem. Rec.* **2015**, *15*, 295-309.

(52) Li X.; Antonietti M. *Chem. Soc. Rev.* **2013**, *42*, 6593-6604.

(53) Wang Y.; Nie Y.; Ding W.; Chen S.; Xiong K.; Qi X.; Zhang Y.; Wang J.; Wei Z. *Chem. Commun.* **2015**, *51*, 8942-8945.

(54) Zhou Y.; Liu C.; Fan S. *J. Mat. Chem. A* **2015**, *3*, 19539-19544.

(55) Kim M.; Hwang S.; Yu J. *J. Mater. Chem.* **2007**, *17*, 1656-1659.

(56) Subramanian V.; Wolf E.; Kamat P. *J. Am. Chem. Soc.* **2004**, *126*, 4943-4950.

(57) Wang Y.; Yao J.; Li H.; Su D.; Antonietti M. *J. Am. Chem. Soc.* **2011**, *133*, 2362-2365.

(58) Su H.; Zhang K.; Zhang B.; Wang H.; Yu Q.; Li X.; Antonietti M.; Chen J. *J. Am. Chem. Soc.* **2017**, *139*, 811-818

(59) Hu S.; Yang L.; Tian Y.; Wei X.; Ding J.; Zhong J.; Chu P. *App. Cat. B* **2015**, *163*, 611-622.

(60) Cai Y.; Li X.; Zhang Y.; Wei X.; Wang K.; Chen J. *Angew. Chem. Int. Ed.* **2013**, *52*, 11822-11825.

(61) Abbas A.; Liu G.; Narita A.; Orosco M.; Feng X.; Müllen K.; Zhou C. *J. Am. Chem. Soc.* **2014**, *136*, 7555-7558.

(62) Saleh M.; Baumgarten M.; Mavrinskiy A.; Schäfer T.; Müllen K. *Macromolecules* **2010**, *43*, 137-143.

(63) Martinelli J.; Watson D.; Freckmann D.; Bardner T.; Buchwald S. *J. Org. Chem.* **2008**, *73*, 7102-7107.

(64) Kim S.; Kim B. *Synthesis* **2009**, *12*, 1963-1968.

(65) Schwab M.; Narita A.; Hernandez Y.; Balandina T.; Mali K.; De Feyter S.; Feng X.; Müllen K. *J. Am. Chem. Soc.* **2012**, *134*, 18169-18172.

(66) Verzhbitskiy I.; De Corato M.; Ruini A.; Molinari E.; Narita A.; Hu Y.; Schwab M.; Bruna M.; Yoon D.; Milana S.; Feng X.; Müllen K.; Ferrari A.; Casiraghi C.; Prezzi D. *Nano Lett.* **2016**, *16*, 3442-3447.

(67) Cao Z.; Kim D.; Hong D.; Yu Y.; Xu J.; Lin S.; Wen X.; Nichols E. M.; Jeong K.; Reimer J. A.; Yang P.; Chang C. J. *J. Am. Chem. Soc.* **2016**, *138*, 8120–8125.

(68) Peng S.; Lee Y.; Wang C.; Yin H.; Dai S.; Sun S. *Nano. Res.* **2008**, *1*, 229–234.

(69) Lee J.; Kim J.; Hyeon T. *Adv. Mater.* **2006**, *18*, 2073–2094.

(70) Stein A.; Wang Z.; Fierke M. A. *Adv. Mater.* **2009**, *21*, 265–293.

(71) Kim H.; Robertson A. W.; Kim S. O.; Kim J. M.; Warner J. H. *ACS Nano* **2015**, *9*, 5947–5957.

(72) Luo J.; Jang H. D.; Huang J. *ACS Nano* **2013**, *7*, 1464–1471.

(73) McEnaney B. *Carbon* **1988**, *26*, 267-274.

(74) Rodríguez-Reinoso F.; Garrido J.; Martín-Martínez J.; Molina-Sabio M.; Torregrosa R. *Carbon* **1989**, *27*, 23-32.

(75) Sing K. Adsorption by Active Carbons. In *Adsorption by Powders and Porous Solids*, 2nd Edition; Rouquerol J.; Rouquerol F.; Llewellyn P.; Maurin G.; Sing K., Eds.; Elsevier: Oxford, 2014; pp 339-360.

(76) Thommes M.; Cychosz K.; Neimark A. Advanced Physcial Adsorption Characterization of Nanoporous Carbons. In *Novel Carbon Adsorbents*; Tascón J., Ed.; Elsevier: Oxford, 2012; pp 111-116.

(77) Blanco López M.; Martinez-Alonso A.; Tascón J. *Carbon* **2000**, *38*, 1177-1182.

(78) Ehrburger P.; Pusset N.; Dziedzinl P. *Carbon* **1992**, *30*, 1105-1109.

(79) Thommes M.; Morlay C.; Ahmad R.; Joly J. *Adsorption* **2011**, *17*, 653-661.

(80) Hamelin A. *J. Electroanal. Chem. Interfac.* **1984**, *165*, 167–180.

(81) Hamelin A.; Lipkowski J. *J. Electroanal. Chem. Interfac.* **1984**, *171*, 317–330.

(82) Somorjai G.; Li Y. *Introduction to Surface Chemistry and Catalysis*, 2nd Edition; J. Wiley & Sons: Hoboken, 2011; pp 390-410, 580-643.

(83) Pramod P.; Soumya C.; Thomas K. G. *J. Phys. Chem. Lett.* **2011**, *2*, 775-781.

(84) Choi H. C.; Shim M; Bangsaruntip S.; Dai H. *J. Am. Chem. Soc.* **2002**, *124*, 9058-9059.

(85) Kong B.; Jung D.; Oh S.; Han C.; Jung H. *J. Phys. Chem. C* **2007**, *111*, 8377-8382.

(86) Gautier L.; Le Borgne V.; Delegan N.; Pandiyan R.; El Khakani M. *Nanotechnology* **2015**, *26*, 045706.

(87) Giovannetti G.; Khomyakov P.; Brocks G.; Karpan V.; van den Brink J.; Kelly P. *hys. Rev. Lett.* **2008**, *101*, 026803.

(88) Peng X.; Tang F.; Copple A. *J. Phys. Condens. Mat.* **2012**, *24*, 075501.

(89) Suzuki S.; Bower C.; Watanabe Y.; Zhou O. *App. Phys. Lett.* **2000**, *76*, 4007-4009.

(90) Liu J.; Li B.; Tan Y.; Giannakopoulos A.; Sanchez-Sanchez C.; Beljonne D.; Ruffieux P.; Fasel R.; Feng X.; Müllen K. *J. Am. Chem. Soc.* **2015**, *137*, 6097-6103.

(91) Fabish T.; Schleifer D. *Carbon* **1984**, *22*, 19-38.

(92) Loufty R. *Carbon* **1986**, *24*, 127-130.

(93) Gileadi E. *Electrode Kinetics for Chemists, Chemical Engineers and Materials Scientists*; Wiley-VCH: New York, 1993.

(94) Lu Q.; Rosen J.; Zhou Y.; Hutchings G. S.; Kimmel Y. C.; Chen J. G.; Jiao F. *Nat. Commun.* **2013**, *5*, 3242.

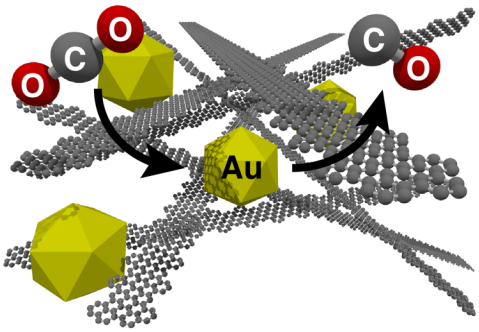
O
C
O
C
O
Au